Comparative Analysis of Single- and Dual-Media Thermocline Tanks for Thermal Energy Storage in Concentrating Solar Power Plants

Carolina Mira-Hernández
School of Mechanical Engineering,
Purdue University,
585 Purdue Mall,
West Lafayette, IN 47907-2088
e-mail: cmira@purdue.edu

Scott M. Flueckiger
School of Mechanical Engineering,
Purdue University,
585 Purdue Mall,
West Lafayette, IN 47907-2088
e-mail: scott.m.flueckiger@gmail.com

Suresh V. Garimella[1]
School of Mechanical Engineering,
Purdue University,
585 Purdue Mall,
West Lafayette, IN 47907-2088
e-mail: sureshg@purdue.edu

A molten-salt thermocline tank is a low-cost option for thermal energy storage (TES) in concentrating solar power (CSP) plants. Typical dual-media thermocline (DMT) tanks contain molten salt and a filler material that provides sensible heat capacity at reduced cost. However, conventional quartzite rock filler introduces the potential for thermomechanical failure by successive thermal ratcheting of the tank wall under cyclical operation. To avoid this potential mode of failure, the tank may be operated as a single-medium thermocline (SMT) tank containing solely molten salt. However, in the absence of filler material to dampen tank-scale convection eddies, internal mixing can reduce the quality of the stored thermal energy. To assess the relative merits of these two approaches, the operation of DMT and SMT tanks is simulated under different periodic charge/discharge cycles and tank wall boundary conditions to compare the performance with and without a filler material. For all conditions assessed, both thermocline tank designs have excellent thermal storage performance, although marginally higher first- and second-law efficiencies are predicted for the SMT tank. While heat loss through the tank wall to the ambient induces internal flow nonuniformities in the SMT design over the scale of the entire tank, strong stratification maintains separation of the hot and cold regions by a narrow thermocline; thermocline growth is limited by the low thermal diffusivity of the molten salt. Heat transport and flow phenomena inside the DMT tank, on the other hand, are governed to a great extent by thermal diffusion, which causes elongation of the thermocline. Both tanks are highly resistant to performance loss over periods of static operation, and the deleterious effects of dwell time are limited in both tank designs.
[DOI: 10.1115/1.4029453]

Keywords: thermocline energy storage, solar thermal energy, molten salt, concentrating solar power, single-medium thermocline, dual-media thermocline

Introduction

CSP is a promising and commercially viable technology for harvesting solar thermal energy at large scale. In a CSP plant, electricity generation occurs through a thermodynamic power cycle, usually a Rankine cycle, which is driven by high-temperature thermal energy obtained by transferring focused solar energy to a heat transfer fluid (HTF). Reliance on direct solar radiation subjects CSP to the inherent variations in weather and cloud conditions and requires cost-effective energy storage technologies to maintain steady power output. Susceptibility to weather transients is a key issue in the development and expansion of sustainable energy technologies [1]. The adoption of TES increases the performance of CSP plants by decoupling demand for electricity generation from solar energy availability [2–5].

Thermocline tanks are sensible-heat TES devices that have been applied in industrial and domestic energy conversion processes [6]. In a thermocline tank, both the cold and hot reserves of HTF are stored in a single tank with buoyancy forces serving to maintain thermal stratification in the vertical direction. Isothermal hot and cold fluid regions become separated by a narrow region of temperature gradient, which is called the thermocline or heat-exchange region [2]. Due to their potential low cost relative to more established two-tank storage methods, molten-salt thermocline tanks are an attractive option for TES in CSP systems [7,8].

In a DMT tank, a low-cost granulated material is added to the tank to reduce the volume of molten salt required to charge the system. In contrast, a SMT tank contains only molten salt. DMT tanks are notionally favored because they have known economical and technical advantages over SMT tanks: The low-cost filler material replaces a large volume of the comparatively more expensive molten salt, with only a marginal reduction in the thermal capacity of the tank. The filler material also acts as a porous-medium flow distributor that dampens unwanted secondary velocities in the tank cross section that may destratify the hot and cold HTF regions. SMT tanks, in contrast, may be more vulnerable to boundary condition variations and entrance effects that induce nonuniform flow phenomena, such as tank-scale mixing eddies. The importance of proper fluid distribution at the inlet is discussed in Refs. [9] and [10].

The thermal behavior of molten-salt DMT tanks has been primarily studied via one-dimensional numerical models [8,11]; a few experimental studies have also been reported [8]. Extensive simulations have been performed to quantify multidimensional thermal and fluid flow behavior inside the tank [12], performance under cyclic operation [13], structural stability of the tank wall

[1]Corresponding author.
Contributed by the Solar Energy Division of ASME for publication in the Journal of Solar Energy Engineering: Including Wind Energy and Building Energy Conservation. Manuscript received July 23, 2014; final manuscript received December 17, 2014; published online January 8, 2015. Assoc. Editor: Nathan Siegel.

[14], and system-level performance in conjunction with a CSP plant model [15].

One disadvantage of DMT tanks is the possibility for mechanical failure by thermal ratcheting [14]. During cyclic operation, the tank wall and the internal filler material undergo differential thermal expansion and contraction. This disparity can lead to separation between the wall and internal filler; reorientation of the filler bed to settle into this annular gap (i.e., interference) results in mechanical stress along the tank wall. If this stress is sufficient for the tank wall material to yield, repeated wall expansions (or "ratchets") may accumulate with each storage cycle until catastrophic failure [14]. Thermal ratcheting cannot occur in the SMT tank design due to the absence of a filler material. The risk of clogging pipes by entrainment of the filler material into the molten-salt flow is also eliminated.

SMT tanks are applied in power conversion technologies beyond CSP applications, such as in industrial refrigeration systems [6] and domestic thermal storage tanks for solar water heaters [16]. In these low-temperature applications, water is used as the storage medium due to its high heat capacitance and low cost. Thermal stratification of water in tanks is a mature heat storage technology, and analytical, numerical, and experimental studies have been previously reported [17–21]. Molten-salt SMT tanks operate at larger temperature differences than water thermocline tanks, undergoing stronger thermal stratification forces; however, the thermal and fluid flow phenomena inside molten-salt SMT tanks for CSP applications have not been directly evaluated against a DMT counterpart through numerical simulation.

Given the nascent state of thermocline tank adoption in CSP systems, the present work assesses the comparative thermal storage performance and behavior of molten-salt DMT and SMT tanks under cyclic operation. In order to separately analyze the dependence of stratification on thermal diffusion across the thermocline and thermal advection due to bulk motion of the molten salt from natural convective currents driven by external heat loss, two thermal boundary conditions are considered on the external tank wall: (1) perfectly adiabatic and (2) heat loss through an insulation layer. The effect of cyclic operation, including periods without salt flow (so-called dwell times), is also evaluated. During these dwell periods, the changes to thermal stratification can be analyzed in the absence of advection due to the bulk motion of molten salt.

Numerical Model

Problem Description. The numerical analysis considers a thermocline tank filled with molten salt and operating between hot and cold HTF sources at 600 °C and 300 °C, respectively. The tank is operated with a discharge power of 25 MWt and is sized to store 12 h of thermal energy (300 MWh). A tank overdesign capacity of 1.5 h is added for simultaneous containment of the desired thermal energy (at high temperature) and the additional thermocline region composed of HTF at cold and transitional temperatures.

The molten salt considered is a commercial eutectic mixture known as solar salt, composed of sodium nitrate (60 wt.%) and potassium nitrate (40 wt.%) that solidifies at 221 °C. The temperature-dependent molten salt physical properties are calculated using the following curve fits derived from experimental data (temperature in Celsius) [22]:

$$\rho_l(T_l) = 2090 - 0.636T_l \tag{1}$$

$$\mu_l(T_l) = 22.714 - 0.120T_l + 2.281 \times 10^{-4}T_l^2 - 1.474 \times 10^{-7}T_l^3 \tag{2}$$

$$k_l(T_l) = 0.443 + 1.9 \times 10^{-4}T_l \tag{3}$$

The specific heat of the molten salt is relatively constant (within ±1.7%) in the operating temperature range and is therefore fixed at a mean value of 1520 kJ/kg K. For the DMT tank, the quartzite rock has a mean particle diameter of 15 mm and a bed porosity of 0.22 [8]. The properties of the quartzite rock are treated as constant, with a specific heat of 830 J/kg K, density of 2500 kg/m^3, and thermal conductivity of 5 W/m K [12,23].

The tank height is fixed to 12 m for both thermocline designs, a practicable value based on a previous design study [24]. The required diameter of the DMT tank to satisfy the energy storage requirement is 14 m. The total volume of the filler bed is 1847 m^3, and the volume of salt is 406 m^3. The required diameter of the SMT tank is 12.85 m and contains 1556 m^3 of molten salt (with no filler). The required mass flow rate of molten salt (54.8 kg/s) is determined from the discharge power, P, as

$$\dot{m}_h = \frac{P}{c_{p,l}(T_h - T_c)} \tag{4}$$

Figure 1 schematically illustrates the geometry and principal components of a thermocline tank.

For nonadiabatic cases, a mineral wool insulation layer is included around the tank geometry to mitigate heat losses to ambient, following the recommendations of a previously reported design and economic analysis that considered similar operating temperatures [24]. Properties of the insulation layer are treated as constant with a specific heat of 835 J/kg K, density of 190 kg/m^3, and thermal conductivity of 0.046 W/m K [25]. The insulation thickness is 0.25 m.

The TES system is connected to the solar field flow loop to collect energy when excess solar energy is available, and alternately to the power block flow loop to deliver stored energy when necessary. Hence, three basic operational modes of the thermocline tank are considered: charge, discharge, and dwell. During the charge process, hot molten salt (carrying energy from the solar field) enters at the top of the tank while cold fluid exits at the bottom (to be heated in the solar receiver). During the discharge process, hot fluid exits from the top (delivering energy for steam generation and consequent power production) while cold fluid returning from the power block enters at the bottom of the tank. During dwell times, there is no flow of the molten salt into or out of the tank. A dwell period is imposed when the thermal storage reaches its energy capacity or the tank energy is depleted.

In actual operation of thermocline TES systems, the frequency and duration of each operational mode depend on the system design, solar energy availability, and electricity demand. Energy collection is subjected to daily and seasonal variations in solar

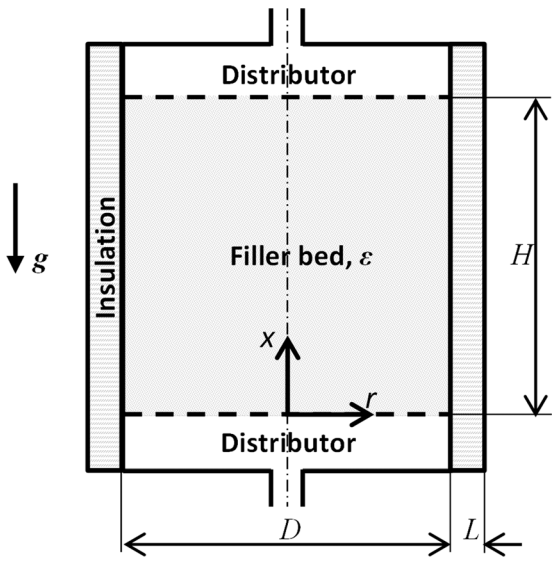

Fig. 1 Schematic illustration of a thermocline tank

radiation, which are highly dependent on the geographic location and meteorological conditions. It is impractical to consider all such possible temporal variations with detailed multidimensional models, and instead, two hypothetical 24 h cycles with equal energy input are chosen to assess the performance of the DMT and SMT tanks. The first cycle includes equal 12 h charge and discharge processes without an intermediate dwell time. The second cycle considers 3 h dwell periods at the beginning and end of the charge cycle; the charge process duration is reduced to 6 h, and the mass flow entering is doubled. The 12 h discharge process is unchanged. The second cycle with dwell time accounts for the energy collection being typically more intense around solar noon, when solar energy availability is usually higher, and the tank becoming saturated to capacity before the end of the day; stored energy is used overnight and the tank is depleted in the morning. Figure 2 illustrates the two cycles.

Governing Equations and Boundary Conditions. The thermal behavior of a thermocline tank is governed by mass, momentum, and energy conservation principles. The fluid flow into the main storage region is limited to low velocities to prevent degradation of thermal stratification. The motion of molten salt inside the DMT tank is expressed by laminar flow equations with Darcy and Forchheimer terms included to account for viscous and inertial momentum dissipation in the porous bed. The mass and momentum conservation equations are stated in terms of the superficial velocity as

$$\frac{\partial(\varepsilon\rho_{\mathrm{l}})}{\partial t}+\nabla\cdot(\rho_{\mathrm{l}}\mathbf{u})=0 \tag{5}$$

$$\frac{\partial(\rho_{\mathrm{l}}\mathbf{u})}{\partial t}+\nabla\cdot\left(\rho_{\mathrm{l}}\frac{\mathbf{uu}}{\varepsilon}\right)=-\varepsilon\nabla p+\nabla\cdot\tilde{\boldsymbol{\tau}}+\varepsilon\rho_{\mathrm{l}}\mathbf{g}-\varepsilon\left(\frac{\mu}{K}\mathbf{u}+\frac{F}{\sqrt{K}}\rho_{\mathrm{l}}|\mathbf{u}|\mathbf{u}\right) \tag{6}$$

where the stress tensor is defined as $\tilde{\boldsymbol{\tau}}=\mu\left(2\tilde{\mathbf{S}}-2/3\mathrm{tr}\left(\tilde{\mathbf{S}}\right)\tilde{\mathbf{I}}\right)$ with the strain rate tensor $\tilde{\mathbf{S}}=1/2\left(\nabla\mathbf{u}+(\nabla\mathbf{u})^{\mathrm{T}}\right)$. The spatial gradient in cylindrical coordinates is $\nabla=\mathbf{e}_r(\partial/\partial r)+\mathbf{e}_\theta(1/r)(\partial/\partial\theta)+\mathbf{e}_x(\partial/\partial x)$. Fluid flow is assumed to be two-dimensional axisymmetric, eliminating all angular functional dependencies. Relations from the literature are used for the permeability, evaluated as $K=d_{\mathrm{s}}^2\varepsilon^3/175(1-\varepsilon)^2$ [26], and for the inertial coefficient, evaluated as $F=1.75/\sqrt{150\varepsilon^3}$ [27]. Governing equations for the SMT tank can be obtained by setting the porosity to unity and considering an infinite permeability.

Inside the DMT tank, the molten salt exchanges thermal energy with the filler bed, which provides sensible storage capacity. Separate energy equations for each phase are required to account for the local thermal nonequilibrium. Viscous dissipation effects are negligible due to low velocities of molten salt and large temperature gradients in the thermocline tank.

$$\frac{\partial\left(\varepsilon\rho_{\mathrm{l}}c_{\mathrm{p,l}}(T_{\mathrm{l}}-T_{\mathrm{c}})\right)}{\partial t}+\nabla\cdot\left(\rho_{\mathrm{l}}\mathbf{u}c_{\mathrm{p,l}}(T_{\mathrm{l}}-T_{\mathrm{c}})\right)=\nabla\cdot(k_{\mathrm{eff}}\nabla T_{\mathrm{l}})+h_i(T_{\mathrm{s}}-T_{\mathrm{l}}) \tag{7}$$

$$\frac{\partial\left((1-\varepsilon)\rho_{\mathrm{s}}c_{\mathrm{p,s}}(T_{\mathrm{s}}-T_{\mathrm{c}})\right)}{\partial t}=-h_i(T_{\mathrm{s}}-T_{\mathrm{l}}) \tag{8}$$

The energy equations are coupled by the volumetric heat transfer rate between the solid and liquid phases due to interstitial convection. The interstitial heat transfer coefficient is computed using the Wakao and Kaguei correlation for fluid flow through a packed bed of spheres ($\mathrm{Nu}_i=6(1-\varepsilon)(2+1.1\mathrm{Re}^{0.6}\,\mathrm{Pr}^{0.33})$) [28]. The filler bed forms an unconsolidated porous medium with minimal contact area between particles. Heat conduction between the solid particles is assumed to be negligible; however, an effective thermal conductivity is used in the liquid-phase energy equation to account for the additional thermal diffusion in the porous medium. The effective thermal conductivity of the solid–liquid mixture is calculated using the relation proposed by Gonzo for medium-density dispersions ($0.15<1-\varepsilon<0.85$) [29]. The curve fit for the molten-salt thermal conductivity is substituted into the correlation to account for the temperature dependence of this property. At the median temperature of 450 °C, the effective thermal conductivity of the filler bed is 4.05 W/m K.

In an actual thermocline tank, distributors are incorporated at the top and bottom to promote uniform flow and hence curtail mixing of hot and cold fluid. In the current study, ideal distribution is assumed, and distributors are omitted from the simulation to simplify the model geometry. The validity of this simplification is supported by the predominance of stratifying buoyancy forces, due to large difference in density between the hot and cold regions. Uniform flow conditions are imposed at the inlet port corresponding to the specific mode of operation. During the charge process, hot molten salt is specified to enter the top of the tank, with uniform inlet velocity u_{h} and temperature T_{h}.

$$T_{\mathrm{l}}|_{x=H}=T_{\mathrm{h}}\qquad u_x|_{x=H}=u_{\mathrm{h}} \tag{9}$$

Cold molten salt exits the tank at the bottom, where a pressure-outlet boundary condition is imposed with backflow temperature T_{c}. During the discharge process, the flow is reversed and cold molten salt is specified to enter at the bottom of the tank with uniform velocity u_{c} and temperature T_{c}.

$$T_{\mathrm{l}}|_{x=0}=T_{\mathrm{c}}\qquad u_x|_{x=0}=u_{\mathrm{c}} \tag{10}$$

The top boundary is modeled as a pressure outlet with backflow temperature T_{h}. During the dwell time, the inlet flow is ceased, and the top and bottom of the filler bed are modeled as adiabatic walls.

The uniform inlet velocities of the salt are set to values that guarantee the required mass flow rate of the hot-side molten salt. The expression for the cold salt velocity during the discharge process is obtained from mass and energy balances around the filler bed.

$$u_{\mathrm{c}}=u_{\mathrm{h}}\left[\varepsilon\left(\frac{\rho_{\mathrm{l,h}}c_{\mathrm{p,l}}}{(1-\varepsilon)\rho_{\mathrm{s}}c_{\mathrm{p,s}}+\varepsilon\rho_{\mathrm{l,h}}c_{\mathrm{p,l}}}\right)\left(1-\frac{\rho_{\mathrm{l,h}}}{\rho_{\mathrm{l,c}}}\right)+\frac{\rho_{\mathrm{l,h}}}{\rho_{\mathrm{l,c}}}\right] \tag{11}$$

where $u_{\mathrm{h}}=\dot{m}_{\mathrm{h}}/(\pi/4)\left(\rho_{\mathrm{l,h}}D^2\right)$.

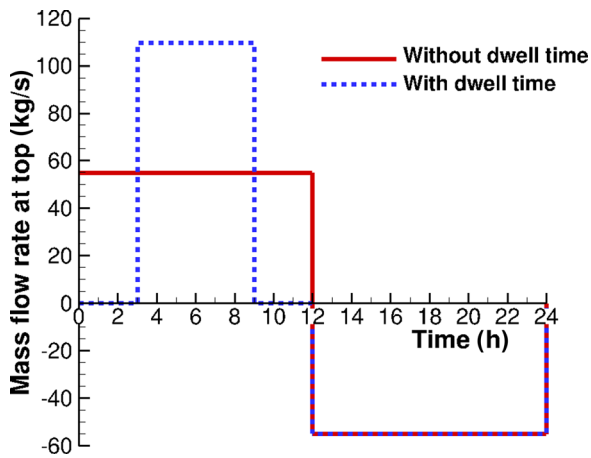

Fig. 2 Mass flow rate into (top) or out of (negative) the top of the thermocline during cyclical operation with and without dwell time

Two alternatives for the external boundary conditions are considered on the cylindrical tank wall. The first condition assumes that the tanks are perfectly adiabatic (the thermal insulation is not included in the simulation). The second condition includes the insulation with an external wall temperature set to the ambient temperature, to simulate a situation of negligible convective thermal resistance with the surrounding air. Heat diffusion is modeled in the insulation layer.

$$T_{\text{ins}}\big|_{r=\frac{D}{2}+L} = T_{\infty} \tag{12}$$

At the tank wall, coupling between the filler bed and the insulation is imposed to guarantee temperature continuity and energy conservation across the interface.

$$T_{\text{ins}}\big|_{r=\frac{D}{2}} = T_{\text{l}}\big|_{r=\frac{D}{2}} \quad k_{\text{ins}}\left.\frac{\partial T_{\text{ins}}}{\partial r}\right|_{r=\frac{D}{2}} = k_{\text{eff}}\left.\frac{\partial T_{\text{l}}}{\partial r}\right|_{r=\frac{D}{2}} \tag{13}$$

Solution Procedure. The governing equations are numerically solved using the finite volume method implemented in the commercial computational fluid dynamics software FLUENT [30]. The two-dimensional domain is discretized into a structured mesh composed of rectangular cells. For the present study, a second-order upwind scheme is used for spatial discretization of velocity components and temperature, and a body force-weighted scheme is used for spatial discretization of the pressure. Transient discretization is performed with a first-order implicit formulation. Pressure–velocity coupling is accomplished through the pressure implicit with splitting of operators (PISO) algorithm [31]. Experimental validation of this numerical model was demonstrated in Ref. [12] with a simulation of a 2.3 MWh DMT tank built by Sandia National Laboratories [8].

An initial temperature distribution is imposed to speed convergence to the time-periodic solution. In the DMT tank, the temperature in the upper half of the filler bed is set to T_{h} (600 °C), and the temperature of the lower half is set to T_{l} (300 °C). In the SMT tank, for which thermal diffusion is slower, an initial thermocline region is included at half the height of the tank in between two isothermal regions at T_{h} and T_{l}; a linear temperature distribution between the hot and cold extremes is imposed across the thermocline region [32]. A one-dimensional, steady-state radial conduction analysis is used to compute an initial temperature field for the insulation. Seven cycles are simulated for each case to obtain the desired time-periodic solution where the temperature field from cycle to cycle deviates less than 0.1%. The time step size for all the simulations of the DMT tank is $\Delta t = 6$ s. A time step size of $\Delta t = 1.2$ s is used for the simulations of the SMT tank, except for the case of an adiabatic tank wall with dwell time in the cycle for which a smaller time step of $\Delta t = 0.6$ s is required to improve numerical stability. For all the simulations, the maximum number of iterations per time step is set to 60 (which ensures that convergence is achieved within each time step). The convergence criteria used for residuals are 10^{-3} for the continuity and momentum equations and 10^{-6} for the energy equation.

For cases with an adiabatic tank wall, mesh sizes of $\Delta r = 0.005D$ in the radial direction and $\Delta x = 0.01H$ in the axial direction are used for both the DMT and SMT tanks. For the SMT tank case with heat loss through the insulation, a radial mesh refinement is required near the wall, due to the relatively high velocities caused by the local cooling. An axial grid refinement is also performed to guarantee an acceptable aspect ratio for the elements near the wall. The ratio between the widths (radial direction) of neighboring cells in the transition region is 1.2, and the aspect ratio of the cells in the near wall region cells is constrained to be 5.0. The details of this locally refined meshing scheme are shown in Fig. 3. This mesh design resolves the flow features near the wall properly and was validated against existing correlations for natural convection on a vertical plate. In the region of mesh

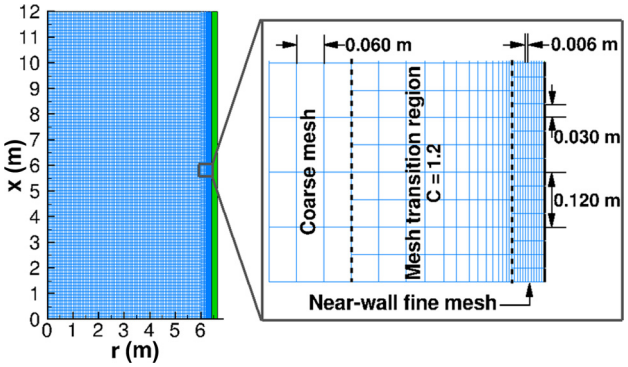

Fig. 3 Schematic illustration of the nonuniform mesh scheme used near the tank wall for the single-medium tank under nonadiabatic wall conditions

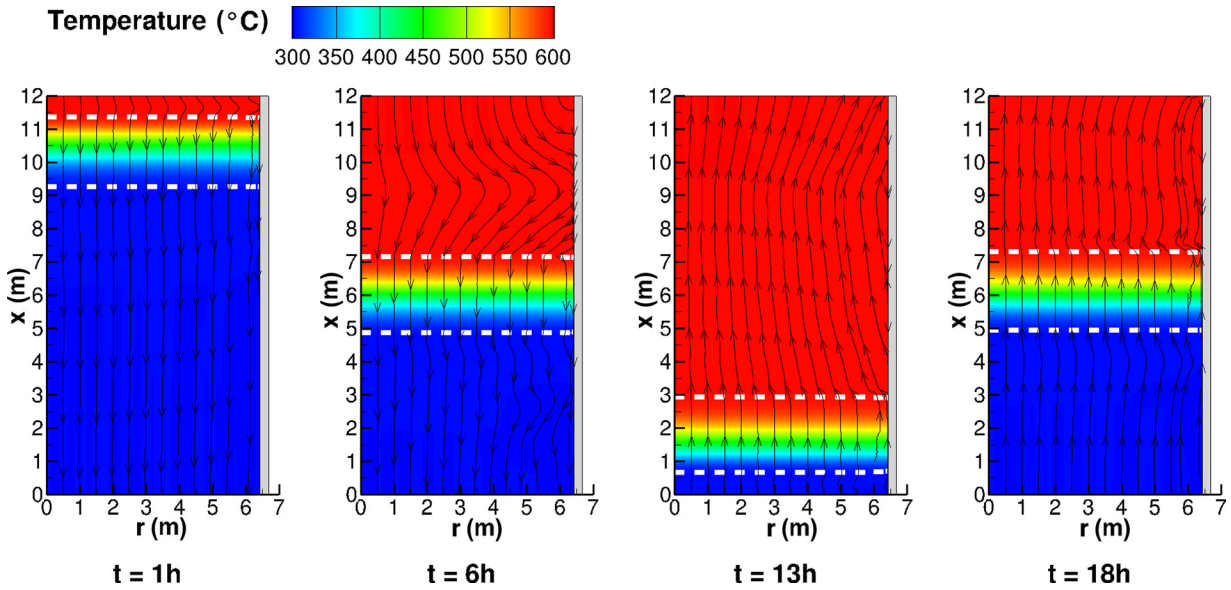

Fig. 4 Instantaneous molten-salt temperature contours and streamlines for the SMT tank with nonadiabatic wall boundary conditions during the cycle without dwell time. The white dashed lines represent the limits of the heat exchange region.

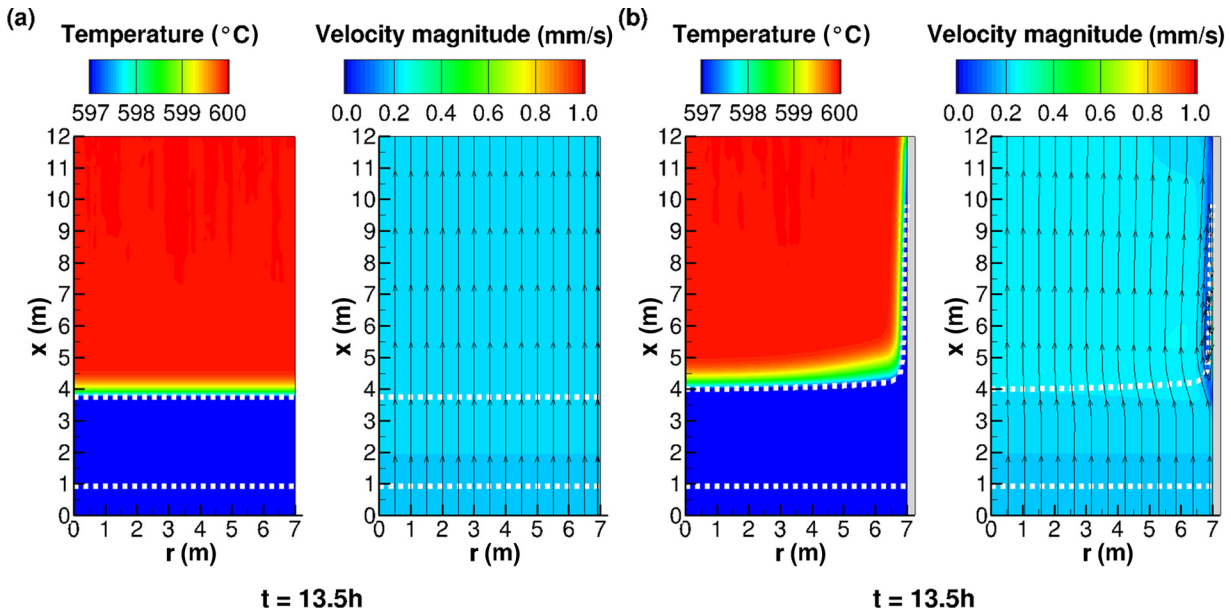

Fig. 5 Instantaneous molten-salt temperature and velocity fields for the DMT tank with (*a*) adiabatic and (*b*) nonadiabatic wall boundary conditions shown at the beginning of the discharge process ($t = 13.5$ h) under time-periodic operation. The white dashed lines represent the limits of the heat exchange region.

refinement, the Courant number is approximately 1.3, which is adequate given the implicit transient solution.

Results and Discussion

The present study compares the performance of two molten-salt thermocline tank concepts, viz., a DMT and a SMT tank, under cyclic operation with and without dwell time. An idealized situation, where the tank wall is adiabatic, serves as the baseline to contrast the behavior in the case of heat loss through the insulation.

Temperature and Velocity Fields. To display the general behavior of a thermocline tank, Fig. 4 presents temperature contours and streamlines in the SMT tank with the nonadiabatic wall boundary condition at different times of the cycle without dwell time. In the figure, the limits of the thermocline (or heat-exchange) region are indicated with white dashed lines. This region is defined as the zone where local temperatures are in the middle 98% of the operational range $0.01 \leq (T - T_c)/(T_h - T_c) \leq 0.99$.

The instantaneous temperature and velocity fields at the beginning of the discharge process are shown in Fig. 5 for the DMT tank and in Fig. 6 for the SMT tank, both for the cycle without dwell time. Stable operation of the thermocline systems results in only a small temperature gradient outside the thermocline region. Therefore, to better illustrate the temperature distribution within the hot salt above the thermocline region, in these figures, the

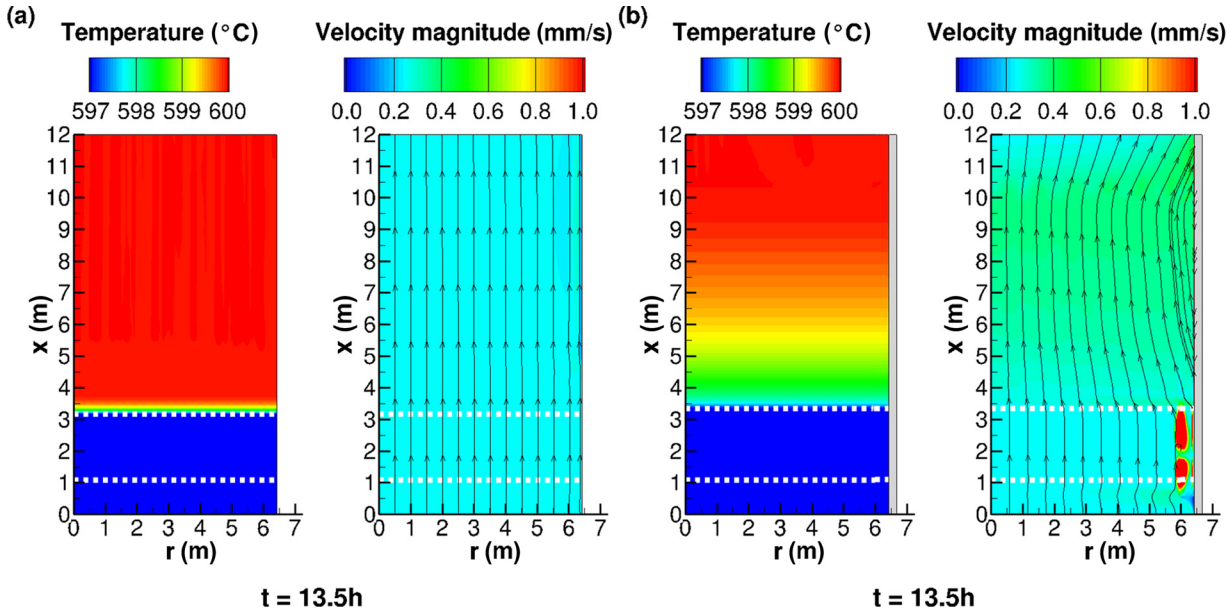

Fig. 6 Instantaneous molten-salt temperature and velocity fields for the SMT tank with (*a*) adiabatic and (*b*) nonadiabatic wall boundary conditions shown at the beginning of the discharge process ($t = 13.5$ h) under time-periodic operation. The white dashed lines represent the limits of the heat exchange region.

range of temperature contours is limited between 597 °C and 600 °C, corresponding to $0.99 \leq (T - T_c)/(T_h - T_c) \leq 1.00$.

Figures 5 and 6 include the results for adiabatic and nonadiabatic tank wall boundary conditions. For adiabatic walls, the flow inside both DMT and SMT tanks is mostly uniform. A thin boundary layer develops in the SMT tank at the wall (though not visible in Fig. 6(*a*)), which is suppressed in the vicinity of the thermocline region due to a dominance of the buoyancy forces over viscous forces. In the DMT tank, the magnitudes of the velocity of hot and cold molten salt differ as a result of the density difference. For both tanks, the temperature field is one-dimensional, but additional thermal diffusion is observed in the DMT tank due to the higher diffusivity of the quartzite filler.

When heat loss from the wall occurs through an insulation layer in the nonadiabatic case, the flow field inside the tanks is perturbed, most notably for the SMT tank (Fig. 6(*b*)). During the charge process, the heavier salt that is being cooled in a narrow region near the wall achieves a relatively high velocity, around 50 mm/s, two orders of magnitude greater than the bulk flow velocity and disturbs the flow at the tank scale (Fig. 4). During the discharge process, an eddy is formed in the hot salt region (Fig. 6(*b*)) because the main flow redirects upward while the colder salt continues to flow downward near the wall. A similar phenomenon is observed in the DMT tank (Fig. 5(*b*)), but the flow disturbance is much weaker. The dissipative forces in the porous medium dampen the eddy that appears during discharge, and the maximum downward velocity near the wall reaches only 0.7 mm/s. Within the thermocline region of high temperature gradient, the dominance of stratifying buoyancy forces causes the flow to be uniform for both thermocline tank designs.

For the nonadiabatic cases, the differences in the predominant thermal transport mechanisms for both tank designs are most evident from the temperature contours. As observed in Fig. 5(*b*), the temperature distribution of the hot salt region in the DMT tank is two-dimensional and is dominated by thermal diffusion. The central core of hot salt maintains a constant high temperature, while the salt cooled near the wall and that near the thermocline region has a lowered temperature. The thermocline region shape is altered and drawn up along the wall. For the SMT tank, as seen in Fig. 6(*b*), the temperature distribution of the hot salt is nearly one-dimensional and is dominated by thermal convective transport that attenuates radial temperature gradients and by stratification that promotes axial temperature gradients. The temperature gradually decreases toward the thermocline region, and it has little variation in the radial direction. While there are some multidimensional hydrodynamic flow disturbances which may not be perfectly captured by the two-dimensional model, the mixing induced by these disturbances, which occur in regions with low temperature gradients, is adequately accounted for in the net thermal behavior.

Figure 7 illustrates the molten-salt temperature and velocity fields during the dwell period when the DMT and SMT tanks are filled with hot fluid. Tank-scale eddies are formed by molten salt flowing downward as it is cooled near the wall. Complex flow structures appear in the thermocline region due to vertical stratification and natural convective currents promoted by the nonuniform temperature difference across the insulation, which create radial flow patterns. The flow disturbance inside the SMT tank is greater than inside the DMT tank; radial temperature gradients are therefore not established in the SMT tank due to mixing. Again, a marked thermal diffusion effect is observed inside the DMT tank.

Effective Thermocline Thickness. The thermocline region separates hot and cold fluid reserves in the tank and is composed of salt at intermediate temperatures. Therefore, expansion of the thermocline region increases the tank volume that is used to store degraded thermal energy, and its temporal evolution along the cycle is an indicator of deterioration of thermal stratification. In the present study, an effective thermocline thickness is defined as the ratio between the volume of the thermocline region and the cross-sectional area of the tank.

$$L_{th} = \frac{V_{th}}{\frac{\pi}{4}D^2} \tag{14}$$

The cyclic evolution of the effective thermocline thickness under the different boundary conditions considered is presented in Fig. 8 for the DMT tank and in Fig. 9 for the SMT tank. As a general observation from the figures, the thermocline region expands faster for cases with heat loss at the wall, and its extent is always equal to or larger than the idealized adiabatic cases.

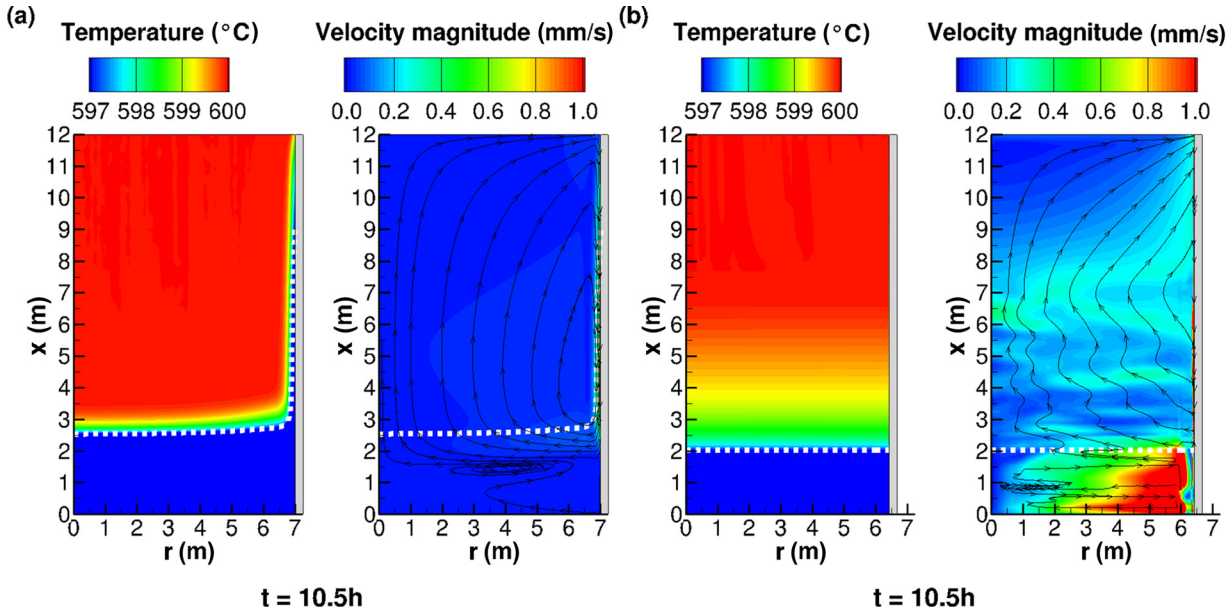

Fig. 7 Instantaneous molten-salt temperature and velocity fields of the (*a*) DMT tank and (*b*) SMT tank with nonadiabatic wall boundary condition during the dwell time when the tank is filled with hot fluid ($t = 10.5$ h). The white dashed lines represent the limits of the heat exchange region.

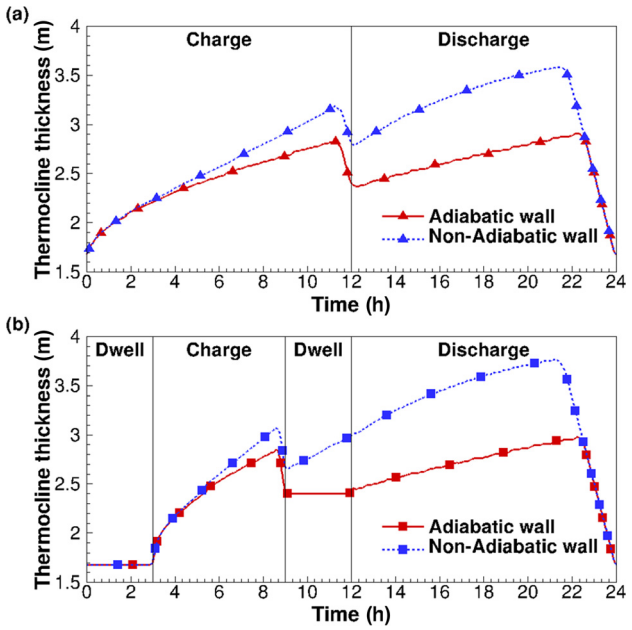

Fig. 8 Effective thickness of the thermocline region inside the DMT tank during the cycles (*a*) without dwell time and (*b*) with dwell time. The solid line illustrates the behavior with an adiabatic wall boundary condition; the dashed line illustrates the behavior with a nonadiabatic wall boundary condition.

The thermocline region inside the SMT tank is thinner compared to the DMT tank. As previously mentioned, this is a consequence of the considerably lower thermal diffusivity of the molten salt compared to the effective properties of the filler bed with quartzite rock (0.18×10^{-6} m^2/s and 1.85×10^{-6} m^2/s, respectively, at the median temperature). Moreover, for nonadiabatic cases in the SMT tank, the salt that is cooled near the wall gets mixed in the large hot region and has a reduced impact on the growth of the thermocline region. On the other hand, in the DMT tank, mixing is weak and the near-wall region is locally cooled to lower temperatures; even though this occurs in a thin region near the wall, it occupies a large volume.

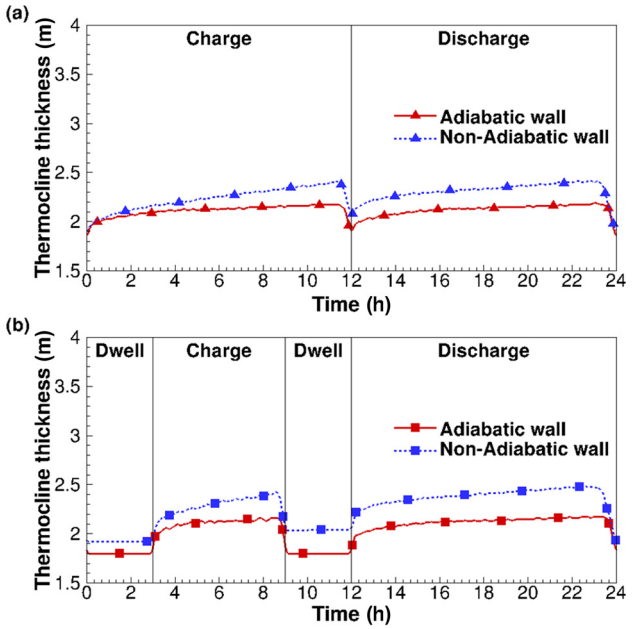

Fig. 9 Effective thickness of the thermocline region inside the SMT tank during the cycles (*a*) without dwell time and (*b*) with dwell time. The solid line illustrates the behavior with an adiabatic wall boundary condition; the dashed line illustrates the behavior with a nonadiabatic wall boundary condition.

The general behavior of the effective thermocline thickness during the cycle without dwell time is similar across the cases considered. The thermocline region exhibits an initial span at the beginning of the charge process, which is a consequence of the overdesign capacity of 1.5 h. A portion of the thermocline always remains inside the tank preventing the discharge of hot salt with too low of a temperature for power generation or cold salt with too high of a temperature for energy collection [15]. During the charge process, the thermocline region travels downward and grows continuously until it reaches the bottom of the tank. At this point, the effective thermocline thickness reduces sharply until the end of the charge process because a fraction of the molten salt at transitional temperatures flows out of the tank. When the flow is reversed for the discharge process, the thermocline region travels upward and expands until it reaches the top; a portion is discharged and causes a sharp decrease in the effective thickness near the end of the process.

During dwell time, when the thermocline is motionless due to the absence of flow into or out of the tank, its expansion rate is dominated by thermal diffusion and mixing currents due to heat loss, but is generally slow relative to expansion during the charge and discharge processes. During the period of dwell before the charge process, when the tank is filled with cold molten salt, expansion of the thermocline region is minimal for both tank designs with adiabatic and nonadiabatic wall boundary conditions. However, for the DMT tank during the dwell time after charge, when the tank is filled with hot molten salt, the thermocline grows notably faster for the nonadiabatic case. The faster rate of thermocline expansion for the hot tank is explained by the local cooling of the filler bed near the tank wall, which is accelerated by the larger temperature difference available to drive heat loss.

Under cyclic operation, the effective thickness of the thermocline region is bounded between a minimum value which occurs at the beginning of the charge process, and a maximum value which occurs when the thermocline region just reaches the top exit during the discharge. The effective height of the tank occupied by salt at transitional temperatures is limited by these values; hence, they serve as indicators of the stratification inside the tank. Table 1 presents the maximum and minimum values of the thermocline thickness during the cycle for the different cases. It is observed that dwell periods in the cycle have a marginally negative effect on the thermal stratification, causing little expansion of the thermocline in both thermocline tank designs. Heat loss through the tank wall has a larger negative effect, which is accentuated in the DMT tank.

Thermal Energy Storage Performance. The outflow temperature during discharge serves as indicator of the magnitude and quality of the energy recovered from the storage system, and its temporal evolution is plotted for the different operational conditions in Fig. 10 for the DMT tank and in Fig. 11 for the SMT tank. The outflow temperature is computed as a mass-weighted average of the temperature exiting at the top. This metric clearly illustrates any disparity in thermocline behavior from an ideal TES system, i.e., one in which thermal energy is recovered at the same hot temperature at which it was stored. The integrated difference from the ideal constant-temperature discharge profile is interpreted as a loss in performance.

For the adiabatic cases, the outflow temperature is constant and equal to the hot salt temperature until molten salt from the thermocline region begins to flow through the top. Since the thermocline region in the DMT tank is thicker, the outflow temperature decreases earlier in the discharge process than in the SMT tank ($t = 22$ h versus $t = 23.5$ h, respectively). The thinner thermocline region within the SMT tank also results in a more abrupt temperature drop compared to the DMT tank.

Table 1 Bounds of thermocline thickness for dual and SMT tanks under time-periodic operation

	DMT tank		SMT tank	
Tank wall boundary condition	Without dwell time (m)	With dwell time (m)	Without dwell time (m)	With dwell time (m)
Adiabatic	1.7–2.9	1.7–3.0	1.8–2.2	1.8–2.2
Nonadiabatic	1.7–3.6	1.7–3.8	1.8–2.4	1.9–2.5

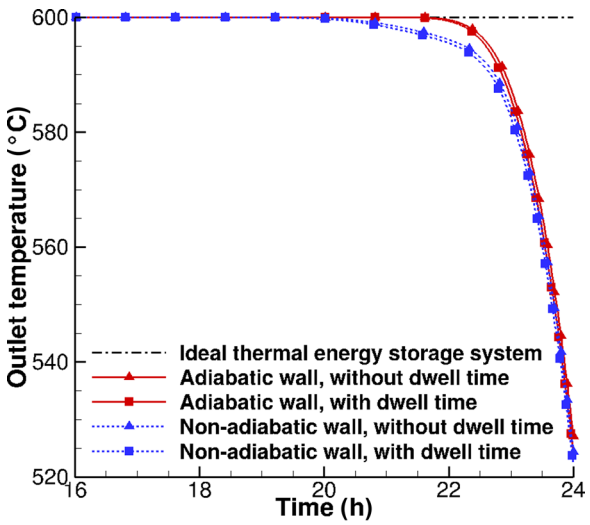

Fig. 10 Outflow temperature history during discharge of the DMT tank

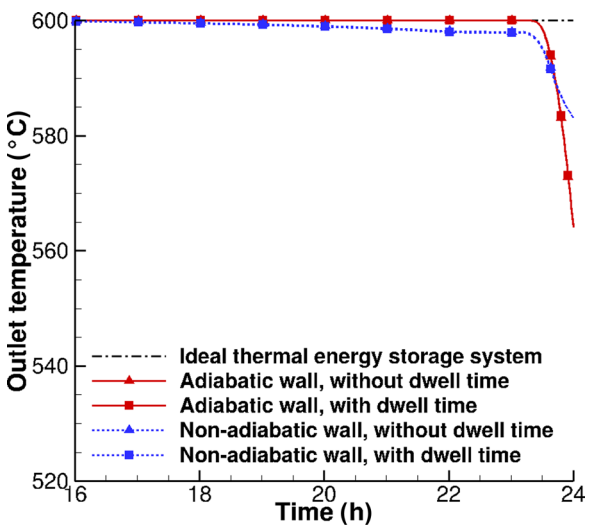

Fig. 11 Outflow temperature history during discharge of the SMT tank

The thermocline tank designs exhibit distinctly different behaviors when heat loss occurs through the insulated tank wall. The discharge temperature profile of the DMT tank is similar to the adiabatic case but with an earlier decrease in outflow temperature ($t = 20$ h) due to the expanded thermocline region. In the SMT tank, outflow temperature decreases slightly at a time much earlier ($t = 16.5$ h) in the discharge process for the nonadiabatic wall (due to the increased mixing inside the hot region of the tank), but exhibits a less sharp drop during the outflow of the thermocline region in the last half hour (due to lengthening of this region).

As previously discussed, dwell time in the cycle reduces performance by allowing destruction of thermal stratification mainly by thermal diffusion and therefore has a greater influence on the DMT tank. Including dwell periods during cyclic operation of the DMT tank has a minor influence on the outflow temperature history. The outflow temperature decreases earlier in the discharge process and remains lower than that of the cycle without dwell time. For the SMT tank, the behavior is virtually identical for both cycles considered.

First- and second-law efficiencies compare the energy and exergy delivered during the discharge process with the quantities stored during the charge process. These efficiencies are, respectively, defined as follows:

$$\eta_{\mathrm{I}} = \frac{E_{\mathrm{out,dis}}}{E_{\mathrm{in,chg}}} = \frac{\int_0^{t_0} \dot{m}_{\mathrm{out,dis}}(T_{\mathrm{out}} - T_{\mathrm{c}})dt}{\dot{m}_{\mathrm{in,chg}}(T_{\mathrm{h}} - T_{\mathrm{c}})t_0} \tag{15}$$

$$\eta_{\mathrm{II}} = \frac{X_{\mathrm{out,dis}}}{X_{\mathrm{in,chg}}} = \frac{\int_0^{t_0} \dot{m}_{\mathrm{out,dis}}[(T_{\mathrm{out}} - T_{\mathrm{c}}) - T_{\mathrm{o}} \ln(T_{\mathrm{out}}/T_{\mathrm{c}})]dt}{\dot{m}_{\mathrm{in,chg}}[(T_{\mathrm{h}} - T_{\mathrm{c}}) - T_{\mathrm{o}} \ln(T_{\mathrm{h}}/T_{\mathrm{c}})]t_0} \tag{16}$$

Table 2 presents the first- and second-law efficiencies of the DMT and SMT tanks for each different boundary condition and cycle. Both tank designs have excellent performance under the evaluated conditions ($\eta_{\mathrm{I}} > 98.34\%$; $\eta_{\mathrm{II}} > 98.18\%$). The inclusion of dwell periods and heat loss through the tank wall causes a drop in efficiency that follows the trends in the outflow temperature and in the phenomena described in previous subsections Temperature and Velocity Fields and Effective Thermocline Thickness. The overall drop in performance is less than 1% for both tank designs compared with the best performance case, in which heat loss and dwell time are absent. For the cases considered, the SMT tank has a marginal advantage due to thermal diffusion being a greater detriment than convection.

Table 3 lists the total heat loss over the cycle for the DMT and SMT tanks for nonadiabatic cases. The total heat loss for both

Table 2 First- and second-law efficiencies for dual and SMT tanks

	DMT tank		SMT tank	
Tank wall boundary condition	Without dwell time	With dwell time	Without dwell time	With dwell time
Adiabatic	$\eta_{\mathrm{I}} = 98.72\%$ $\eta_{\mathrm{II}} = 98.60\%$	$\eta_{\mathrm{I}} = 98.62\%$ $\eta_{\mathrm{II}} = 98.50\%$	$\eta_{\mathrm{I}} = 99.68\%$ $\eta_{\mathrm{II}} = 99.67\%$	$\eta_{\mathrm{I}} = 99.69\%$ $\eta_{\mathrm{II}} = 99.67\%$
Nonadiabatic	$\eta_{\mathrm{I}} = 98.45\%$ $\eta_{\mathrm{II}} = 98.30\%$	$\eta_{\mathrm{I}} = 98.34\%$ $\eta_{\mathrm{II}} = 98.18\%$	$\eta_{\mathrm{I}} = 99.55\%$ $\eta_{\mathrm{II}} = 99.51\%$	$\eta_{\mathrm{I}} = 99.52\%$ $\eta_{\mathrm{II}} = 99.48\%$

Table 3 Total heat loss over one 300 MWh storage cycle for thermocline tanks with nonadiabatic wall condition

Cycle	DMT tank (MWh)	SMT tank (MWh)
Without dwell time	1.002	0.921
With dwell time	1.000	0.922

tank designs is similar, approximately 0.3% of the heat storage capacity of 300 MWh. This total heat loss is equivalent to an average heat flux of 80 W/m^2, which is consistent with experimental values reported for two-tank molten salt storage systems [5]. The low heat losses explain the similarity in efficiencies of adiabatic and nonadiabatic cases.

Conclusions

Two types of molten-salt thermocline tanks for a TES system are explored through numerical simulation; a conventional DMT tank composed of molten salt and quartzite rock, and a SMT tank filled only with molten salt. The thermal performance is comparatively assessed under 24-h storage cycles with and without periods of dwell and under adiabatic and nonadiabatic external boundary conditions.

For nonadiabatic cases, the total heat lost through the wall during the cycle is negligible compared to the heat storage capacity, but instead influences the overall efficiency by affecting the internal flow pattern and outflow temperature during discharge. Heat loss through the wall causes thermal-buoyancy-induced flow nonuniformities due to the cooling of molten salt near the tank wall. In the SMT tank, large-scale eddies are induced by high velocities near the wall; in contrast, nonuniformities are damped in the DMT tank by drag inside the porous media. Stronger tank-scale mixing in the SMT tank (for nonadiabatic cases) causes a slight drop in the outflow temperature early in the discharge process of the SMT tank, reducing the overall efficiency. However, increased thermal diffusion in the DMT tank (due to the higher thermal diffusivity of the quartzite rock) alternatively reduces the storage efficiency by elongating the vertical thermocline region compared to the SMT tank. Under the conditions of operation considered in this study, both tanks have excellent thermal performance in terms of first- and second-law efficiencies, but the tradeoff between reduced thermal diffusion and convective mixing favors the SMT tank. The expansion of the thermocline region by diffusion during dwell time is small, with minor effects on the behavior of the DMT tank and almost negligible effects in the SMT tank.

The present study focused on the thermal and fluid flow phenomena inside DMT and SMT tanks for CSP plants and showed that the tradeoffs in thermal performance are minor under realistic operating conditions. Therefore, a practical decision regarding the preferred design is likely to rest on economics.

Acknowledgment

This paper is based upon work supported in part under the US–India Partnership to Advance Clean Energy-Research (PACE-R) for the Solar Energy Research Institute for India and the United States (SERIIUS), funded jointly by the U.S. Department of Energy (Office of Science, Office of Basic Energy Sciences, and Energy Efficiency and Renewable Energy, Solar Energy Technology Program, under Subcontract DE-AC36-08GO28308 to the National Renewable Energy Laboratory, Golden, CO) and the Government of India, through the Department of Science and Technology under Subcontract IUSSTF/JCERDC-SERIIUS/2012 dated 22nd Nov. 2012. The first author acknowledges the financial support provided by the Colombia-Purdue Institute (CPI) and the Colombian Department for Science, Technology and Innovation (Colciencias).

Nomenclature

c_p = specific heat (J/kg K)
C = size ratio between adjacent cells
d_s = diameter of filler granules (m)
D = diameter of the thermocline tank (m)
E = energy (J)
$\boldsymbol{e}$ = unit vector
F = inertial coefficient
$\boldsymbol{g}$ = gravitational acceleration (m/s^2)
h_i = volumetric interstitial convection coefficient (W/m^3 K)
H = height of the thermocline tank (m)
$\tilde{\boldsymbol{I}}$ = identity tensor
k = thermal conductivity (W/m K)
K = permeability (m^2)
L = insulation thickness (m)
L_{th} = effective thermocline thickness (m)
$\dot{m}$ = mass flow rate (kg/s)
Nu_i = interstitial Nusselt number ($\mathrm{Nu}_i = h_i d_s^2/k_l$)
p = pressure (Pa)
P = power (W)
Pr = Prandtl number ($\mu_l c_{p,l}/k_l$)
r = radial coordinate (m)
Re = Reynolds number ($\mathrm{Re} = \rho_l d_s|\mathbf{u}|/\mu_l$)
$\tilde{\boldsymbol{S}}$ = strain rate tensor (s^{-1})
t = time (s)
t_0 = half-cycle period (s)
T = temperature (°C)
u = velocity component (m/s)
$\boldsymbol{u}$ = velocity vector (m/s)
v = traversal speed of the heat exchange region (m/s)
V = volume (m^3)
x = axial coordinate (m)
X = exergy (J)
Δr = cell size in radial direction (m)
Δx = cell size in axial direction (m)

Greek Symbols

ε = porosity
η = efficiency
μ = viscosity (Pa s)
ρ = density (kg/m^3)
$\tilde{\boldsymbol{\tau}}$ = stress tensor (Pa)

Subscripts

c = low inlet discharge temperature
chg = charge process
dis = discharge process
eff = effective
h = high inlet charge temperature
in = inlet
ins = insulation
l = molten salt
out = outlet
r = radial direction
s = solid filler
th = thermocline region
x = axial direction
θ = tangential direction
∞ = surroundings
0 = reference state
I = first law of thermodynamics
II = second law of thermodynamics

References

[1] Ibrahim, H., Ilinca, A., and Perron, J., 2008, "Energy Storage Systems: Characteristics and Comparisons," Renewable Sustainable Energy Rev., **12**(5), pp. 1221–1250.

[2] Gil, A., Medrano, M., Martorell, I., Lázaro, A., Dolado, P., Zalba, B., and Cabeza, L. F., 2010, "State of the Art on High Temperature Thermal Energy Storage for Power Generation. Part 1: Concepts, Materials and Modellization," Renewable Sustainable Energy Rev., **14**(1), pp. 31–55.

[3] Tamme, R., Laing, D., and Steinmann, W. D., 2004, "Advanced Thermal Energy Storage Technology for Parabolic Trough," ASME J. Sol. Energy Eng., **126**(2), pp. 794–800.

[4] Luzzi, A., Lovegrove, K., Filippi, E., Fricker, H., Schmitz-Goeb, M., Chandapillai, M., and Kaneff, S., 1999, "Techno-Economic Analysis of a 10 MWe Solar Thermal Power Plant Using Ammonia-Based Thermochemical Energy Storage," Sol. Energy, **66**(2), pp. 91–101.

[5] Herrmann, U., Kelly, B., and Price, H., 2004, "Two-Tank Molten Salt Storage for Parabolic Trough Solar Power Plants," Energy, **29**(5–6), pp. 883–893.

[6] Dincer, I., 2002, "On Thermal Energy Storage Systems and Applications in Buildings," Energy Build., **34**(4), pp. 377–388.

[7] Kearney, D., Herrmann, U., Nava, P., Kelly, B., Mahoney, R., Pacheco, J., Cable, R., Potrovitza, N., Blake, D., and Price, H., 2003, "Assessment of a Molten Salt Heat Transfer Fluid in a Parabolic Trough Solar Field," ASME J. Sol. Energy Eng., **125**(2), pp. 170–176.

[8] Pacheco, J. E., Showalter, S. K., and Kolb, W. J., 2002, "Development of a Molten-Salt Thermocline Thermal Storage System for Parabolic Trough Plants," ASME J. Sol. Energy Eng., **124**(2), pp. 153–159.

[9] Zurigat, Y., Liche, P., and Ghajar, A., 1991, "Influence of Inlet Geometry on Mixing in Thermocline Thermal Energy Storage," Int. J. Heat Mass Transf., **34**(1), pp. 115–125.

[10] Chung, J. D., Cho, S. H., Tae, C. S., and Yoo, H., 2008, "The Effect of Diffuser Configuration on Thermal Stratification in a Rectangular Storage Tank," Renewable Energy, **33**(10), pp. 2236–2245.

[11] Li, P., Van Lew, J., Karaki, W., Chan, C., Stephens, J., and Wang, Q., 2011, "Generalized Charts of Energy Storage Effectiveness for Thermocline Heat Storage Tank Design and Calibration," Sol. Energy, **85**(9), pp. 2130–2143.

[12] Yang, Z., and Garimella, S. V., 2010, "Thermal Analysis of Solar Thermal Energy Storage in a Molten-Salt Thermocline," Sol. Energy, **84**(6), pp. 974–985.

[13] Yang, Z., and Garimella, S. V., 2013, "Cyclic Operation of Molten-Salt Thermal Energy Storage in Thermoclines for Solar Power Plants," Appl. Energy, **103**, pp. 256–265.

[14] Flueckiger, S. M., Yang, Z., and Garimella, S. V., 2012, "Thermomechanical Simulation of the Solar One Thermocline Storage Tank," ASME J. Sol. Energy Eng., **134**(4), p. 041014.

[15] Flueckiger, S. M., Iverson, B. D., Garimella, S. V., and Pacheco, J. E., 2014, "System-Level Simulation of a Solar Power Tower Plant With Thermocline Thermal Energy Storage," Appl. Energy, **113**(86–96), pp. 86–96.

[16] Abdoly, M., and Rapp, D., 1982, "Theoretical and Experimental Studies of Stratified Thermocline Storage of Hot Water," Energy Conversation Manage., **22**(3), pp. 275–285.

[17] Yoo, H., and Pak, E., 1993, "Theoretical Model of the Charging Process for Stratified Thermal Storage Tanks," Sol. Energy, **51**(6), pp. 513–519.

[18] Han, Y. M., Wang, R. Z., and Dai, Y. J., 2009, "Thermal Stratification Within the Water Tank," Renewable Sustainable Energy Rev., **13**(5), pp. 1014–1026.

[19] Bahnfleth, W. P., and Song, J., 2005, "Constant Flow Rate Charging Characteristics of a Full-Scale Stratified Chilled Water Storage Tank With Double-Ring Slotted Pipe Diffusers," Appl. Therm. Eng., **25**(17–18), pp. 3067–3082.

[20] Al-Najem, N., 1993, "Degradation of a Stratified Thermocline in a Solar Storage Tank," Int. J. Energy Res., **17**(3), pp. 183–191.

[21] Wood, R. J., Al-Muslahi, S. M., O'Callaghan, P. W., and Probert, S. D., 1981, "Thermally Stratified Hot Water Storage Systems," Appl. Energy, **9**(3), pp. 231–242.

[22] Pacheco, J. E., Ralph, M. E., Chavez, J. M., Dunkin, S. R., Rush, E. E., Ghanbari, C. M., and Matthews, M. W., 1995, "Results of Molten Salt Panel and Component Experiments for Solar Central Receivers: Cold Fill, Freeze/Thaw, Thermal Cycling and Shock, and Instrumentation," Sandia National Laboratories Report No. SAND94-2525.

[23] Côté, J., and Konrad, J., 2005, "A Generalized Thermal Conductivity Model for Soils and Construction Materials," Can. Geotech. J., **458**, pp. 443–458.

[24] EPRI, 2010, "Solar Thermocline Storage Systems: Preliminary Design Study," Palo Alto, CA.

[25] Pilato, L., 2010, *Phenolic Resins: A Century of Progress*, Springer, New York.

[26] Beckermann, C., and Viskanta, R., 1988, "Natural Convection Solid/Liquid Phase Change in Porous Media," Int. J. Heat Mass Transf., **31**(1), pp. 35–46.

[27] Krishnan, S., Murthy, J. Y., and Garimella, S. V., 2004, "A Two-Temperature Model for the Analysis of Passive Thermal Control Systems," ASME J. Heat Transfer, **126**(4), pp. 628–637.

[28] Wakao, N., and Kaguei, S., 1982, *Heat and Mass Transfer in Packed Beds*, Gordon and Breach Science Publishers, New York.

[29] Gonzo, E. E., 2002, "Estimating Correlations for the Effective Thermal Conductivity of Granular Materials," Chem. Eng. J., **90**(3), pp. 299–302.

[30] ANSYS, 2011, "Fluent 14.5.0," Canonsburg, PA.

[31] Issa, R., 1986, "Solution of the Implicitly Discretised Fluid Flow Equations by Operator-Splitting," J. Comput. Phys., **62**(1), pp. 40–65.

[32] Mira-Hernández, C., Flueckiger, S., and Garimella, S., 2014, "Numerical Simulation of Single-and Dual-media Thermocline Tanks for Energy Storage in Concentrating Solar Power Plants," Energy Proc., **49**, pp. 916–926.